ISSN 1063-7842, Technical Physics, 2013, Vol. 58, No. 10, pp. 1469–1475. © Pleiades Publishing, Ltd., 2013.
Original Russian Text © V.V. Lisenkov, V.V. Osipov, V.V. Platonov, 2013, published in Zhurnal Tekhnicheskoi Fiziki, 2013, Vol. 83, No. 10, pp. 78–84.

PHYSICAL SCIENCE OF MATERIALS

Interaction of the Radiation of the High-Power Ytterbium-Fiber Laser with Inhomogeneous Dielectric Targets

V. V. Lisenkov[a, b]*, V. V. Osipov[a], and V. V. Platonov[a]

[a] *Institute of Electrophysics, Ural Branch, Russian Academy of Sciences, ul. Amundsena 106, Yekaterinburg, 620016 Russia*
[b] *Ural Federal University, ul. Mira 19, Yekaterinburg, 620002 Russia*
**e-mail: lisenkov@iep.uran.ru*

Received June 22, 2012

Abstract—The action of the radiation of the ytterbium-fiber laser ($\lambda = 1.07$ μm) on the $Nd^{3+}Y_2O_3$ target with nonuniform transparency in the course of the nanopowder production is studied. It is demonstrated that the laser irradiation leads to an extremely rough surface with the stalagmite roughness due to a relatively large melting depth. The resulting powder consists of two fractions. The first fraction (99% of the total mass of the powder) consists of nanoparticles with a mean size of 29 nm (BET data). The second fraction consists of micro- and submicroparticles that represent circular drops condensed from the melt and shapeless debris of the target. The peaks on the diameter distribution of the drops at 2, 8, and 80 μm are determined by different effects. The laser heating of the inhomogeneous target with the nonlinear refractive index is numerically analyzed. It is demonstrated that the melting of the target is initiated at a mean laser power of 700 W, a power density of 5.6×10^5 W/cm^2, and an irradiation time of 150 μs.

DOI: 10.1134/S1063784213100150

INTRODUCTION

High-power fiber lasers are widely employed in various technologies instead of alternative lasers due to a relatively high efficiency, small size of the focal spot, high power density, reliability, and compactness. The fiber lasers are most widely used in metal cutting. For example, it is demonstrated in [1] that an ytterbium-fiber laser provides the cutting of alloyed steel sheets with a thickness of 4 mm at a rate that is four times greater than the rate provided by the CO_2 laser of the same power. However, the CO_2 laser is superior with respect to cutting quality when the thickness of the metal sheets increases to 20 mm. Similar results can be found in [2], where close rates of the cutting of thick steel sheets are reported for both lasers and the higher cutting quality of the CO_2 laser is mentioned. It is theoretically demonstrated in [3] that the efficiency of the CO_2 laser in cutting of the stainless-steel sheets with a thickness of greater than 8 mm is higher than the efficiency of the fiber laser. A fiber laser is characterized as a promising tool for microcutting of metals in [4].

Note few works on the interaction of the fiber-laser radiation with dielectric targets. In particular, an ytterbium-fiber laser is used in [5] for the production of the nanopowder from the yttrium-stabilized zirconium oxide. Several aspects of the fiber laser application in comparison with the CO_2 laser application are discussed. At an identical mean radiation power, the nanopowder production rate and power consumption are 23 g/h and 87 kW h/kg, respectively, for the fiber laser. The production rate and power consumption are 18 g/h and 250 kW h/kg, respectively, for the repetitively pulsed CO_2 laser. It is also mentioned that the application of the fiber laser allows a decrease in the specific surface of the nanopowder from 79 to 42 m^2/g and the regime of dagger melting in which a rough surface of the target is formed and the nanopowder production rate decreases.

It is fair to say that early and far from the best results for the CO_2 laser were chosen for the comparison.

The aforementioned facts stimulate the further study and the purpose of this work is the analysis of the interaction of the radiation of the ytterbium laser with inhomogeneous (with respect to transparency) targets in the nanopowder production.

1. EXPERIMENTAL RESULTS

Figure 1 demonstrates the block diagram of the experimental setup for the production of the 1% $Nd:Y_2O_3$ nanopowder. The radiation of an LS-07N laser *1* is focused by optical head *2* on target *4* that is placed inside evaporation chamber *3*. The target is fixed on a stage that provides the rotation and translation for the uniform evaporation. The beam moves along the surface of the target at a speed of 35 cm/s. First, the target is placed in such a way that the surface of the target corresponds to the center of the laser beam waist, so that the beam spot on the target is 200 μm at a focal length of the optical head of 200 mm. The laser intensity distribution at the beam waist is close to the Gaussian distribution. The target moves upwards when the material is consumed. Atmospheric-pressure air is pumped through the evapora-

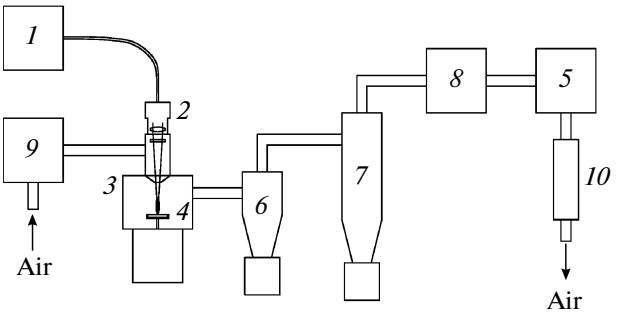

Fig. 1. Block diagram of the setup for the nanopowder production with the aid of the ytterbium-fiber laser: (*1*) fiber laser, (*2*) optical head, (*3*) evaporation chamber, (*4*) target, (*5*) pump, (*6*) cyclone, (*7*) filter for the collection of the nanopowder, (*8*) output filter, and (*9*) input filter.

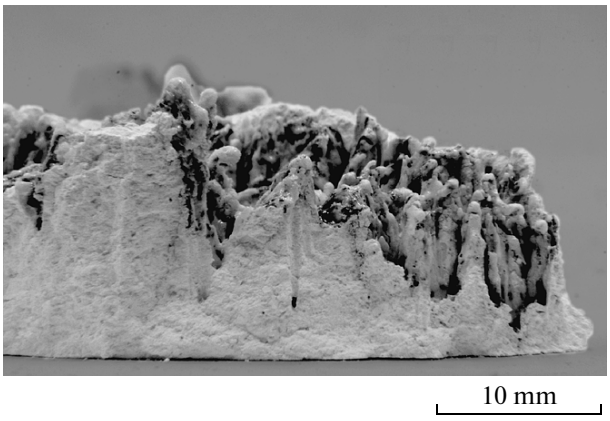

Fig. 2. Photograph of the target after evaporation.

tion chamber using pump *5* at a volume flow rate of 6.3 m^3/h that is measured with the aid of rotameter *10*. The nanoparticles formed in the laser plume are brought to paper filter *7* by the air flow. Cyclone *6* filters out large drops and debris of the target. Input filter *9* provides air cleaning from room dust, and output filter *8* provides final air cleaning for the atmospheric emission. The targets for evaporation are made of commercially available Y_2O_3 and Nd_2O_3 powders with a characteristic particle size of several microns that are mechanically mixed at relative contents of 99 and 1 mol %, respectively. Then, the mixture is compacted using a single-axis press at a force of 50 kN. The resulting cylinders with a diameter of 65 mm and a height of 19 mm are sintered in air at a temperature of 1350°C for 5 h.

Under such conditions, a target with a mass of 130 g is completely spent at a fiber-laser-irradiation time of 90 min. The target is partially evaporated and destroyed (about 50%), and the remaining part becomes nonevaporable. The amount of the nanopowder (23 g) that is collected in the paper filter is two times less than the amount in the experiment with the evaporation of the same target using the radiation of an LAERT CO_2 laser [6]. Thus, the nanopowder production rate for the fiber laser (15 g/h) is also two times less than the production rate for the CO_2 laser. However, new efforts are aimed at an increase in the efficiency of the nanopowder production. In the course of evaporation, the roughness of the surface of the target increases and dips and stalagmite-like peaks are formed (Fig. 2). Thus, the target surface profile indirectly indicates the regime of dagger melting, which is in agreement with the assumption from [5]. In addition, the power density of the laser radiation focused on the stalagmite slope is less and the reflection coefficient is greater than the corresponding quantities for the laser radiation incident on a more horizontal surface of the stalagmite peak or a dip between the stalagmites. On the one hand, this circumstance leads to a lower evaporation rate for the stalagmite slopes and, on the other hand, a part of the substance that is evaporated from the dips may settle on the stalagmites. Both effects lead to a decrease in the nanopowder production rate.

For the study of the morphology and sizes of the particles from the large fractions, the nanopowder from the cyclone is used for multistage sedimentation in isopropyl alcohol. Thus, the nanoparticles can be separated from the large sediment particles whose relative content is about 4%. The BET measurements show that specific surfaces of the powders from the sediment and suspension are 3.4 and 41.0 m^2/g, respectively. The mean size of the particles in the fractions is estimated using the known formula

$$d_{\mathrm{BET}}[\mu\mathrm{m}] = 6/(\rho S), \qquad (1)$$

where ρ is density (g/cm^3) and S is specific surface (m^2/g). The mean sizes of the particles in the nanofraction and sediment are 29 and 350 nm, respectively. Note that the nanopowder in the sediment may lead to the overestimation of the specific surface of the sediment and, hence, underestimation of the mean size.

The study of the sediment powder using an Olympus BX51 optical microscope shows that it consists of circular drops and shapeless debris. Figure 3 shows the distribution function of the drops with respect to the size. The drops exhibit a relatively large scatter of the sizes. The sizes of the largest and smallest drops are about 100 and 1 μm, respectively. Three peaks at 2, 8, and 80 μm are clearly seen on the distribution. In our opinion, the peaks are related to three effects that are involved in the formation of the drops.

The sizes of most debris range from 1 to 10 μm but the largest sizes are up to 150 μm.

The comparison of the above data and the results obtained using a repetitively pulsed CO_2 laser with the same mean power under the same experimental conditions makes it possible to draw the following conclusions.

(i) The nanopowder production rate in the experiments with the ytterbium laser radiation for which the

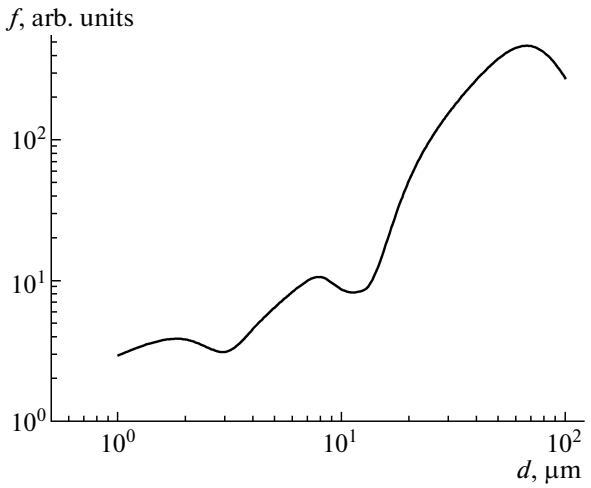

Fig. 3. Distribution function of the drops with respect to size.

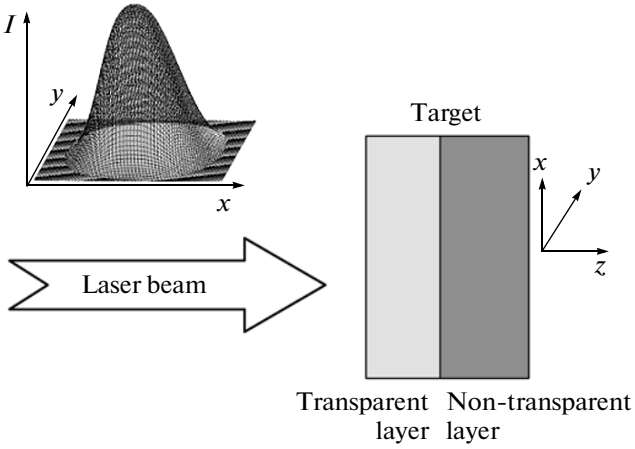

Fig. 4. Geometrical configuration of the problem. The upper inset shows the shape of the laser radiation intensity at the focal spot.

targets are semitransparent is lower than the production rate for the CO_2 laser radiation for which the targets are opaque.

(ii) The evaporation of the semitransparent target leads to a rough surface, earlier destruction, and lower yield of the powder.

(iii) The nanopowder contains large particles with a diameter of about 100 μm.

Below, we discuss these conclusions but it is clear that the presence of large particles is difficult to interpret. Apparently, the effect that leads to the formation of such particles differs from the corresponding effect in the experiments with the CO_2 laser. In this regard, we numerically analyze the dynamics of the thermal processes in the target.

2. RESULTS OF CALCULATIONS

The evaporation of the targets made of refractory oxides with the aid of a pulsed CO_2 laser is experimentally and theoretically studied in [6–8]. Note that the interaction of the radiation of an ytterbium-fiber laser with such targets needs to be additionally studied.

In our opinion, the main difference between the two lasers lies in a tenfold difference of the radiation wavelengths and the corresponding difference of the optical constants of the substances under study. For example, the typical penetration depth of the CO_2-laser radiation with a wavelength of 10.6 μm in the yttrium oxide is several microns whereas the penetration depth of the radiation of the ytterbium-fiber laser with a wavelength of 1.07 μm in the yttrium oxide single crystal is more than 30 cm. However, the presence of macro- and microdefects in the crystals leads to a multifold decrease in the penetration depth. Such a scenario corresponds to the laser synthesis of the yttrium oxide nanoparticles with the aid of a fiber laser, when the opaque evaporated target consists of particles with sizes of 1–10 μm that are partially sintered to each other. After multiple beam passages, the surface of the target is covered with a molten layer with a thickness of 200 μm that is more transparent for the laser radiation. Thus, a variation in optical transparency of the near-surface layer of the target can be related to several specific features of the evaporation dynamics of the target in the presence of the fiber-laser irradiation.

We employ a numerical model from [7] in which the 3D heat-conduction equation is solved:

$$\frac{\partial T}{\partial t} = \chi(T)\Delta T + \frac{Q}{c(T)}. \quad (2)$$

Here, χ is the thermal diffusivity, c is the heat capacity, and Q is the 3D heat source that is generated by the laser radiation

$$Q = \alpha I(x, y, z, t), \quad (3)$$

where α is the absorption coefficient of laser radiation and $I(x, y, z, t)$ is the laser intensity distribution in the medium given by

$$I(x, y, z, t) = (1 - R)I_0(x, y)\exp(-\alpha z). \quad (4)$$

Here, $I_0(x, y)$ is the intensity distribution at the focal spot (see inset to Fig. 4) and R is the reflection coefficient represented as

$$R = \frac{(n-1)^2 + \left(\frac{\alpha\lambda}{4\pi}\right)^2}{(n+1)^2 + \left(\frac{\alpha\lambda}{4\pi}\right)^2}, \quad (5)$$

where n is the refractive index and λ is the wavelength. Using the results of [9], we represent the dependence of coefficient α on temperature T as

$$\alpha(T) = \alpha_0 \exp\left(\frac{T - 300}{300}\xi\right), \quad (6)$$

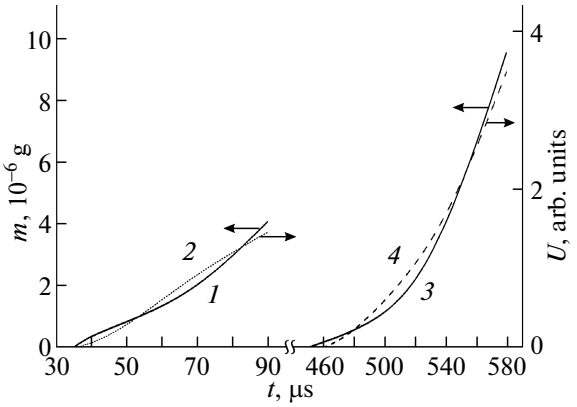

Fig. 5. Dynamics of the initial stage of evaporation for (*1*, *2*) the opaque target at $\alpha_0 = 1.7 \times 10^5$ cm^{-1} and (*3*, *4*) the semitransparent ceramic sample at $\alpha_0 = 23$ cm^{-1}: (*1*) and (*3*) calculated curves of the evaporated mass and (*2*) and (*4*) emission oscillograms.

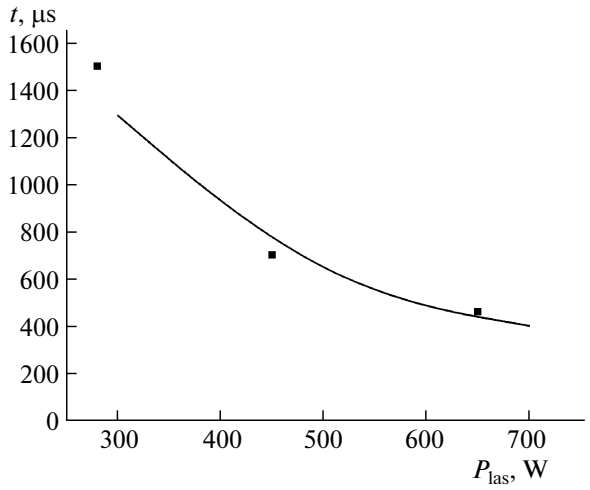

Fig. 6. Plots of the evaporation starting moment vs. laser power for the semitransparent ceramic sample at $\alpha_0 = 23$ cm^{-1}: (solid line) calculated curve and (squares) experimental data.

where α_0 is the absorption coefficient at room temperature (300 K) and ξ is the material constant. In the calculations, we choose such a material constant that coefficient $\alpha(T_m)$ at melting point T_m is equal to α_m that is discussed below. We employ the thermophysical constants from [10, 11].

Figure 4 presents the geometrical configuration of the problem. The laser beam that propagates along the z axis is incident on the xy surface of the target that consists of two layers. The outer layer with a thickness of 0.1 mm represents a relatively transparent melt (light-gray color in Fig. 4). The second (opaque) layer that exhibits a significantly higher absorption coefficient consists of pressed microparticles (dark-gray color in Fig. 4). In several specific cases that are discussed below, we assume that the target is completely homogeneous. In the calculations, parameter α_0 can be varied whereas parameter α_m is constant, since it corresponds to the liquid phase.

Unfortunately, parameters α_m and α_0 cannot be measured in the experiments with the opaque target that is used for the nanopowder production. In a series of the test calculations, we employ the data on the radiation absorption for the Nd:Y_2O_3 ceramic samples with different transparencies that are obtained by A.N. Orlov using the method from [12, 13]. The results of these calculations are compared with the experimental results. In most cases, we use the sample whose absorption coefficient α_0 at wavelength $\lambda = 1.07$ μm is 24 cm^{-1}.

The calculation model is correct if the calculated results coincide with the following experimental data: (i) ablation (volume of crater) for a radiation pulse duration of 10^{-3} s and static target; (ii) delay time of the laser plume, which is close to the starting time of the boiling regime; and (iii) luminance of the laser plume, which must be proportional to the evaporated mass in the first approximation.

We assume that the constants in formula (6) are valid if the experimentally observed tendencies can be interpreted. One of the tendencies is the dependence of the evaporation starting time on the laser pulse power (Fig. 5). The solid curve shows the calculated results, and the squares show the experimental time moments at which the laser plume emerges. It is seen that the difference of the calculated and experimental results is no greater than 10%. Good agreement of the ablation results obtained from the measurements of the crater volumes (two of them are presented in Fig. 6) makes it possible to assume that the above procedure allows the correct analysis of the ablation in the crater on the target. The data are presented in Fig. 7 as the time dependences of the evaporated mass that are in reasonable agreement with the experimental oscillograms of the integral radiation intensity of the laser plume.

With allowance for the experimental results, the above approach was used for the calculation of parameter α_0 of the opaque Nd:Y_2O_3 target. The best agreement with the emission oscillograms is obtained for $\alpha_0 = 1.7 \times 10^3$ cm^{-1} (Fig. 7, curves *3*, *4*). Note that the experimentally detected signal at the initial stage is described using a function that is close rather than identical to the linear function of the evaporated mass. Therefore, we do not expect exact coincidence of the experimental oscillograms and calculated results.

Thus, parameter α_0 for the opaque part of the two-layer target is estimated to be 1.7×10^3 cm^{-1}. We employ $\alpha_0 = 10$ cm^{-1} for the transparent melt based on

the results for the ceramic samples with similar morphology [13].

Figure 8 shows the dynamics of the temperature field in the two-layer target for radiation powers of 700 and 500 W (panels (a) and (b), respectively). At the initial stage, the less transparent region in the vicinity of the interface is heated due to a significant difference of the absorption coefficients. Then, the thermal wave propagates toward the surface of the target. The reason lies in the heat conduction and the consequent heating of the regions that are adjacent to the inhomogeneity where parameter α increases in accordance with expression (6). In the region that is closer to the surface of the target (along the z axis), the laser intensity is higher and the conditions for the positive feedback of parameters T and α are satisfied. Hence, this region intercepts the laser radiation and shields the inhomogeneity. This circumstance leads to the displacement of the temperature maximum toward the surface of the target.

It is seen that the energy deposited to the target increases with time and the temperature maximum increases and moves toward the surface of the target (i.e., the motion of the thermal wave is observed). At a radiation power of 700 W, the temperature maximum reaches a melting point of 2740 K inside the target at a time moment of about 140 μs and depth of about 30 μm. This leads to a stepwise variation in the density in the melting region and the cleavage of the corresponding fragment of the target due to significant mechanical stress. Figure 9a presents the photograph of such a crater and the corresponding profile. The crater is surrounded with a cleavage region with breaking along the crystallite interfaces. The profile with gentle slopes at the edges shows that the depth of the region is slightly greater than 30 μm, which is in good agreement with the calculated results. Note that the depth of the central part with steep slopes (up to 430 μm) is determined by the subsequent evaporation of the target material.

At a radiation power of no greater than 500 W (Fig. 8b), the temperature maximum that is higher than the melting point is reached at the surface of the target. In this case, the melting process is started at a delay of about 225 μs on the surface of the target and the specific features related to the cleavage are not expected. Figure 8b shows such a crater. Note the absence of cleavages and significant breastwork related to the displacement of the melt in the presence of excess vapor pressure of the target, which indicate the surface melting and evaporation of the target.

The temperature distributions that are calculated using the above model allow assumptions on the effects related to the formation of drops and the trimodal distribution (Fig. 3). Figure 9 shows the cross section of a homogeneous target immediately prior to boiling. Note the presence of two characteristic regions. The first one is the melt region with a typical depth of 50–100 μm depending on specific conditions

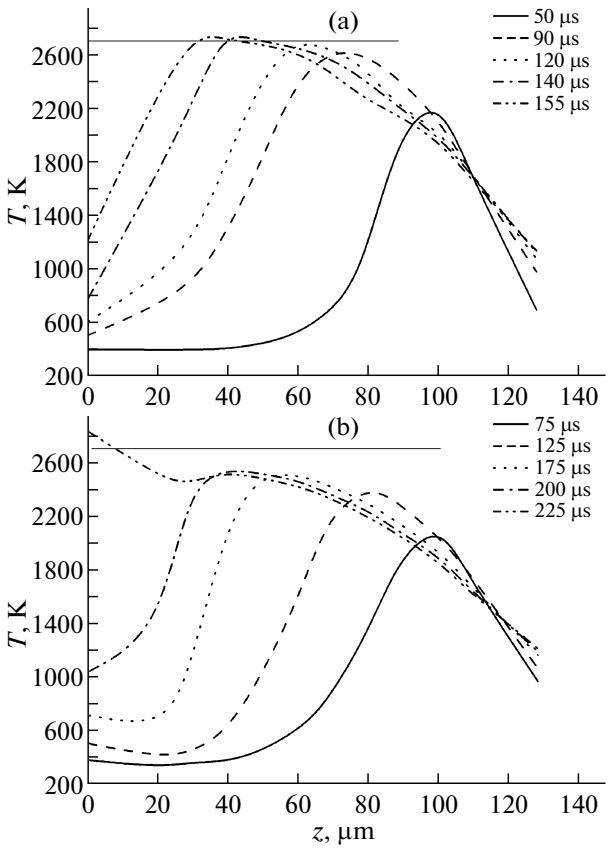

Fig. 7. Plots of the temperature maximum vs. depth for the two-layer target at several time moments for radiation powers of (a) 700 and (b) 500 W with the horizontal lines corresponding to the Y_2O_3 melting point.

(light-gray color in Fig. 9). The second region is the region of the overheated liquid in a metastable state whose typical size is about 2 μm (dark-gray color in Fig. 9). The embryos of the vapor phase are formed in this region. In such a vapor bubble, the pressure is sufficiently high for the ejection of liquid drops when the bubble reaches the surface. Such an evaporation effect is known as the phase explosion [14]. The size of the drops must be about 1 μm (i.e., comparable with the depth of the metastable region). The depth of the metastable region (about 2 μm) corresponds to the first peak on the distribution function of the drops (Fig. 3). Larger drops result from the melting in the thermal wave inside the target with the subsequent surface cleavage that causes the melt splashing. The calculated results (Fig. 8a) show that the typical size of the liquid phase that is formed inside the solid target (7–10 μm) corresponds to the second peak. The largest drops are formed owing to the ejection of hot air from the porous part of the target through the melt layer whose thickness (50–100 μm) approximately corresponds to the third peak on the distribution function (80 μm).

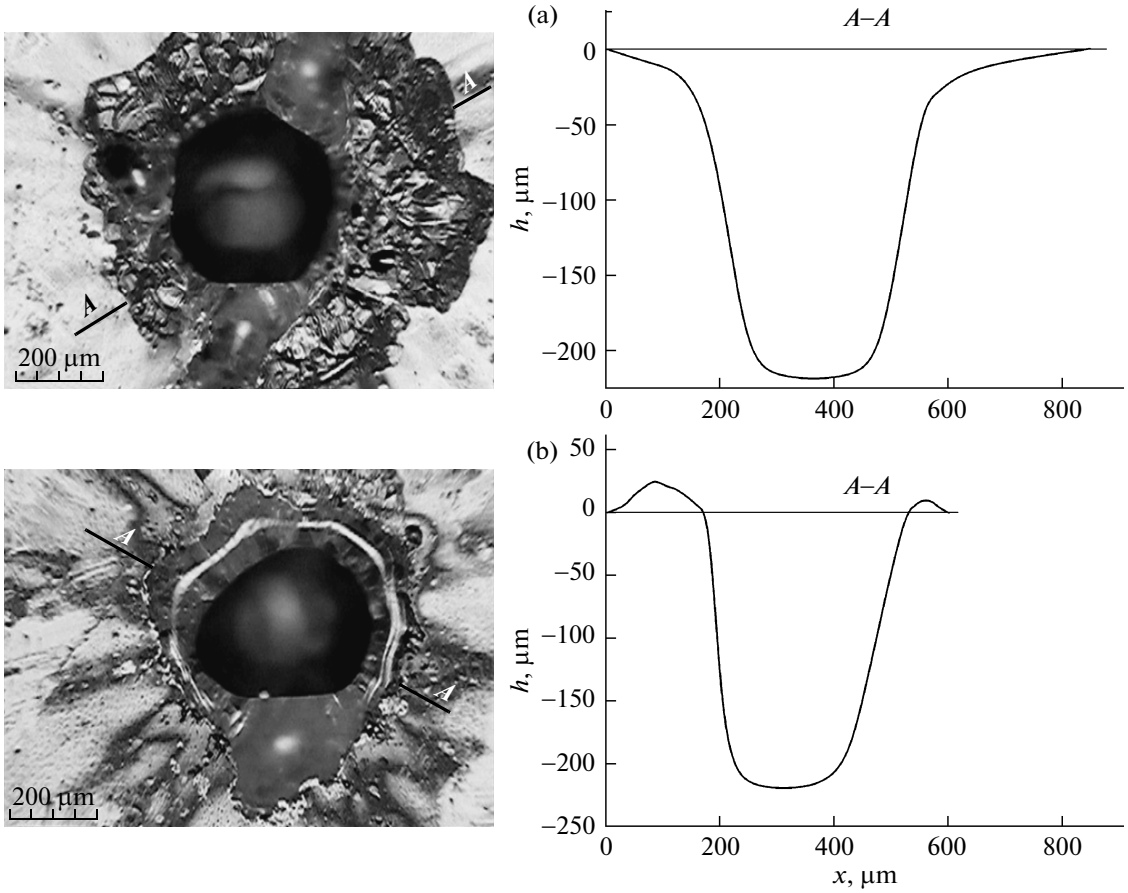

Fig. 8. (Left-hand panels) Photographs of the craters on the surface of the target and (right-hand panels) profiles along the *A–A* cross sections on the photographs (a) in the presence and (b) in the absence of cleavages.

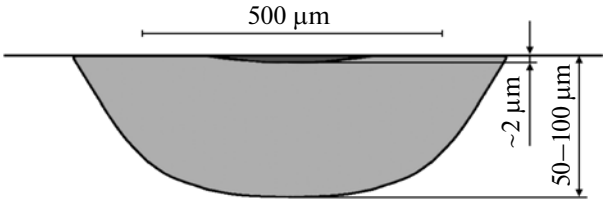

Fig. 9. Typical configuration of the melt region prior to evaporation in the Y_2O_3 target.

CONCLUSIONS

The analysis of the irradiation of the Nd:Y_2O_3 targets with nonuniform transparency using the ytterbium-fiber laser yields the following results.

(i) Extremely rough surface of the target resulting from the evaporation is related to the melting at a relatively large depth and the development of stalagmite-like roughness.

(ii) At a power density of 1.5×10^6 W/cm^2 and a mean power of the fiber laser of 600 W, the above effect leads to the nanopowder production rate that is lower than that for the CO_2 laser of the same power for which the target under study is opaque. Note that the work aimed at an increase in the efficiency is in progress.

(iii) The sedimentation makes it possible to divide the resulting powder into two fractions. The first one (99% of the total mass of the powder) consists of the nanoparticles with a mean size of 29 nm (BET data). The second fraction consists of micro- and submicroparticles that represent circular drops condensed from the melt and shapeless debris of the target. The optical microscopy of the drops with a diameter of greater than 1 μm shows that the size distribution exhibits peaks at 2, 8, and 80 μm determined by different physical effects.

(iv) We developed a numerical model that makes it possible to calculate the dynamics of temperature fields in the Nd:Y_2O_3 targets with nonuniform transparency. In particular, it is demonstrated that the temperature maximum of the wave can be higher than the melting point of the target at a mean laser power of 700 W, power density of 5.6×10^5 W/cm^2, and irradiation time of greater than 150 μs. In this case, a stepwise increase in the pressure in the melting region and the partial cleavage are obtained.

ACKNOWLEDGMENTS

This work was supported by the Russian Foundation for Basic Research (project no. 11-08-00005a) and the Programs of the Presidiums of the Russian Academy of Sciences and Ural Branch, Russian Academy of Sciences.

REFERENCES

1. P. Leibinger, Stahlmarkt **60** (7), 40 (2010).
2. V. B. Shulyat'ev, Doctoral Dissertation (Novosibirsk, 2011).
3. A. V. Zaitsev, O. B. Kovalev, and E. M. Smirnova, *Proceedings of the 4th All-Russia Conference on Interaction of Highly Concentrated Energy Flows with Materials in Advanced Technologies and Medicine, Novosibirsk, 2011*, pp. 94–97.
4. K. F. Kleine and K. G. Watkins, Proc. SPIE **4974**, 184 (2003).
5. Yu. A. Kotov, O. M. Samatov, M. G. Ivanov, et al., Tech. Phys. **56**, 652 (2011).
6. V. V. Osipov, V. V. Platonov, and V. V. Lisenkov, Kvantovaya Elektron. (Moscow) **39**, 541 (2009).
7. V. V. Osipov, Yu. A. Kotov, et. al., Laser Phys. **16**, 116 (2006).
8. V. V. Osipov, V. V. Lisenkov, and V. V. Platonov, Tech. Phys. Lett. **37**, 49 (2011).
9. Yu. K. Danileiko, A. A. Manenkov, A. M. Prokhorov, et al., Zh. Eksp. Teor. Fiz. **63**, 1032 (1972).
10. *Handbook of Physical Quantities*, Ed. by I. S. Grigoriev and E. Z. Meilikhov (CRC Press, Boca Raton, 1997).
11. V. L. Balkevich, *Technical Ceramics* (Stroiizdat, Moscow, 1984).
12. S. N. Bagaev, V. V. Osipov, et al., Kvantovaya Elektron. (Moscow) **38**, 840 (2008).
13. S. N. Bagayev, V. V. Osipov, et. al., Opt. Mater. **31**, 740 (2009).
14. *Synthesis of Nanosized Materials by Impact of Intense Flows on Substance*, Ed. by A. V. Bulgakov, N. M. Bulgakova, et al. (Inst. Teplofiz. SO RAN, Novosibirsk, 2009).

Translated by A. Chikishev